scientific reports

Check for updates

OPEN

Computational molecular characterization of a novel *SLC20A2* variant associated with primary familial brain calcification

Shih-Chun Lan[1], Yu-Sung Huang[2], Jia-Yin Tsai[2], Min-Yu Lan[3,4,5], Yuh-Ju Sun[2]✉ & Yung-Yee Chang[3,4]✉

***SLC20A2*, encoding human type III sodium-dependent phosphate transporter 2 (*h*PiT2), is the gene most frequently associated with primary familial brain calcification (PFBC). The mechanism by which a *SLC20A2* mutation causes phosphate transporter dysfunction may depend on the functional region of *h*PiT2 being affected. We presented clinical and brain imaging data of a patient with idiopathic brain calcification. Genetic testing detected a novel, de novo and in silico-predicted deleterious variant, c.1891 C>T (p.Pro631Ser), in *SLC20A2*. Computational simulations revealed that, compared to the wild type, this variant *h*PiT2 was associated with a higher root mean square deviation in molecular dynamics, a smaller value with a wider range for the kink angle of transmembrane helix 8 (TM8), and a less flexible TM8 structural conformation. These molecular characteristics were also observed in the known pathogenic missense variants in the TM8 of *h*PiT2. The pathogenicity of the novel *SLC20A2* variant p.Pro631Ser is supported by the computational simulations for molecular characteristics of the variant *h*PiT2. The findings also highlight the role of TM8 helix in maintaining normal *h*PiT2 functions.**

Keywords Molecular dynamics simulation, Primary Familial brain calcification, Sodium-dependent phosphate transporter, *SLC20 A2*, P631S variant

Abbreviations

ACMG-AMP	American College of Medical Genetics and Genomics and Association of Molecular Pathology
hPiT2	Human sodium-dependent phosphate transporter 2
MD	Molecular dynamics
PFBC	Primary familial brain calcification
P_i	Inorganic phosphate
PiT2	Type III sodium-dependent phosphate transporter 2
RMSD	Root mean square deviation
TM	Transmembrane
TmPiT	Thermotoga maritima sodium-dependent phosphate transporter
WT	Wild type

Primary familial brain calcification (PFBC), previously known as idiopathic basal ganglia calcification, bilateral striatopallidodentate calcinosis or Fahr's disease, is a disorder characterized by abnormal brain calcification. The calcified lesions that are hyperdense on CT images are located primarily in the bilateral basal ganglia, with varying extents of involvement in the dentate nuclei, thalami, subcortical white matter and cerebral cortex[1]. The diagnosis of PFBC requires the exclusion of biochemical abnormalities, infectious diseases, exposure to toxic

[1]School of Medicine, National Taiwan University College of Medicine, Taipei, Taiwan. [2]Institute of Bioinformatics and Structural Biology, National Tsing Hua University, Hsinchu, Taiwan. [3]Department of Neurology, Kaohsiung Chang Gung Memorial Hospital, and Chang Gung University College of Medicine, Kaohsiung, Taiwan. [4]Center for Parkinson's Disease, Kaohsiung Chang Gung Memorial Hospital, Chang Gung University College of Medicine, Kaohsiung, Taiwan. [5]Center for Mitochondrial Research and Medicine, Kaohsiung Chang Gung Memorial Hospital, Chang Gung University College of Medicine, Kaohsiung, Taiwan. ✉email: yjsun@life.nthu.edu.tw; changyy7@gmail.com

agents and inherited metabolic disorders (e.g., mitochondrial diseases) that may be associated with abnormal brain calcification.

PFBC is heterogeneous in its inheritance patterns and causative genes. Earlier studies identified four genes (*SLC20 A2*, *PDGFB*, *PDGFRB*, and *XPR1*) associated with PFBC in an autosomal dominant inheritance pattern, accounting for approximately 55% of PFBC patients[2]. Later studies have also suggested that biallelic mutations in *MYORG*[3], *JAM2*[4], *CMPK2*[5] and *NAA60*[6] can lead to PFBC. *SLC20A2* is the gene most frequently associated with PFBC (denoted PFBC-*SLC20A2*), with mutations accounting for 50% of all familial cases[7,8].

SLC20A2 encodes type III sodium-dependent phosphate transporter 2 (PiT2), which plays a vital role in maintaining the homeostasis of inorganic phosphate (P_i). As a member of the PiT family, PiT2 consists of two domains, the intracellular soluble domain and the transmembrane (TM) domain. The TM domain of human PiT2 (*h*PiT2) shares high sequence homology with various species, such as *Thermotoga maritima* (*Tm*PiT), with 39% identity and 62% similarity[9]. Previously, we modeled the *h*PiT2 TM domain on the basis of the *Tm*PiT–Na/P_i complex structure[9]. The *h*PiT2 TM domain contains four highly conserved motifs, namely, GΦNDΦ, GxxxxGxxVxxT, PΦSxT and IxxxWΦ (x, any amino acid; Φ, hydrophobic residue), which are vital for the functional and conformational changes of PiT[9–11]. Loss-of-function mutations of the gene, especially those affecting the TM domain, tend to impair the transporter's ability to take up P_i into the cell and cause abnormal depositions of calcium phosphate in the brain[12]. On the other hand, the mechanisms by which *SLC20A2* mutations cause P_i transporter dysfunctions may depend on the functional regions of *h*PiT2 that are affected[9]. For instance, the pathogenic variant D28N affects the sodium-binding residue D28 in one of the P_i–2Na–binding sites, resulting in reduced P_i uptake while retaining P_i-binding affinity. In contrast, the variant W626R affects a tryptophan in the middle of TM8 helix, leading to dysfunction of TM8 conformational changes and impeding opening/closing of the PiT2 inner gate.

PFBC caused by *de novo SLC20A2* mutations is rare. To our knowledge, only two PFBC cases with *de novo* single nucleotide mutations in *SLC20A2* have been reported previously[13,14]. Here, we present a case of PFBC with a novel and *de novo* missense *SLC20A2* variant that affects the TM8 helix. Given that a positive correlation for the variant among the affected familial members was unfeasible, we evaluated the effects of this variant on *h*PiT2 molecular characteristics using computational modeling and simulations. Four other *SLC20A2* missense variants affecting TM8, which either caused PFBC clinically or impaired P_i uptake in *Tm*PiT, were included for comparison. We found that the novel variant exhibited adverse effects on *h*PiT2 conformational changes and stability, similar to known pathogenic variants.

Methods

Genetic testing and in Silico analysis of variants

The study was approved by the Chang Gung Memorial Hospital Institutional Review Board (No.201702186B0) and all participants provided informed consent. All methods were performed in accordance with the relevant guidelines. The details of whole-exome sequencing and genetic variant analysis are described in Additional File 1. In brief, the exome library was captured via a Roche KAPA HyperExome Plus Kit (Roche Sequencing Solutions), and sequencing was performed on a NovaSeq X Plus (Illumina). After sequencing adaptors and low-quality bases were trimmed, read mapping and variant calling were performed using the Burrows–Wheeler Aligner and Genome Analysis Toolkit.

Variants of PFBC-causative genes, including *SLC20A2*, *PDGFB*, *PDGFRB*, *XPR1*, *MYORG*, *JAM2*, *CMPK2* and *NAA60*, were prioritized. Next, only variants that were either reported as "pathogenic" or "likely pathogenic" in ClinVar or predicted to alter the coding proteins were considered. Variants with allele frequencies > 0.001 in any population of any population in the genome database were discarded. Multiple in silico prediction tools have been utilized to predict the pathogenicity of missense variants. The reported variant was confirmed by Sanger sequencing.

Initial structure of the hPiT2 model

The TM domain of *h*PiT2, which contains 12 TM helices, was modeled based on the *Tm*PiT structure[9]. When the soluble domain region (residues 238 to 479) of *h*PiT2, located between TM5 and TM6 of the TM domain, was modeled using AlphaFold3[15], the secondary structure prediction revealed a per-residue confidence score (pLDDT) below 50. We therefore excluded the soluble domain and used only the remaining TM helices for the molecular dynamics (MD) simulation. The *h*PiT2 variants, including V624E, P631S, W626 A, W626R, and S637R, were prepared using the same approach. V624E, W626R and S637R are the missense variants which were identified previously in PFBC patients[7,16–18] and all of them, like P631S, are located in the TM8 helix. The residue W626 in *h*PiT2 corresponds to W378 in *Tm*PiT. The *Tm*PiT mutant W378 A lacks P_i binding affinity[9], suggesting that the ability of the W626 A variant of *h*PiT2 to bind Pi might also be disrupted.

The structural models of wild-type (WT) *h*PiT2 and its variants were embedded into the same membrane system using the Membrane Builder of CHARMM-GUI[19–22]. This system consisted of a lipid mixture of phosphatidylethanolamine (POPE) and phosphatidylcholine (POPC) in a 1:1 ratio with a water layer and 100 mM NaCl. The dimensions of the MD simulation system were $140 \times 140 \times 111$ Å^3. The force fields applied were ff14SB[23], and the water model TIP3P was used with tLEaP from AmberTools22[24].

Molecular dynamics simulation

Each MD simulation of *h*PiT2 complexes was performed with AMBER22[24] with three independent repeats. The first minimization constrains all atoms of the protein, and the water and lipids are minimized. In the second minimization, the backbone of the protein was constrained, and the side chains of the protein, water, and lipid were minimized. In the third minimization, the whole simulation system was optimized without any constraints.

These minimizations are calculated in 2500 steps of the steepest descent and then 2500 steps of the conjugate gradient. The simulation systems were then heated from 0 K to 300 K in 100 ps and equilibrated via the NVT ensemble calculation method in 100 ps. Finally, the production is performed in 200 ns from the NPT ensemble calculation method, in which the total number of atoms is fixed at 300 K and 1 atm.

Measurement of the TM8 helix bending angle

The kink angles of TM8 in WT and *h*PiT2 variants were determined by calculating the angle between two center-of-mass vectors that represent the upper (residue 626–631) and lower (residue 632–637) halves of TM8. Kink angle analysis was performed using CPPTRAJ of AmberTool22[24], and only the Cα atoms were considered for the measurement.

Results

Case presentation and genetic testing results

A 48-year-old Taiwanese woman with a history of anxiety disorder and insomnia presented with an insidious onset of generalized muscle stiffness, slow limb and trunk movements, and intermittent involuntary facial and limb movements for 1 year. Additional symptoms included cognitive decline, apathy, impaired verbal fluency and gait disturbance. She did not have any family history of neurodegenerative disorders (Fig. 1A).

On neurological examination, the patient was alert and oriented. A brief cognitive function screening was performed. The Montreal Cognitive Assessment score was 20/30 (normal ≥26), the Mini-Mental State Examination score was 29/30, and the Cognitive Abilities Screening Instrument score was 87.4/100. Multiple primitive reflexes were present. Her speech was slow, hypophonic and aprosodic. Neurological examination revealed unsmooth eye pursuit, generalized hyperreflexia, and hypomimia but orolingual dyskinesia, axial and appendicular rigidity, global hypokinesia and limb dystonia. The plantar reflexes were flexor bilaterally. The cerebellar and sensory systems were normal. Her gait was narrow and stable, but her stride length and arm swings were decreased. Brain CT revealed symmetric calcification in the dentate, bilateral basal ganglion and periventricular and subcortical white matter (Fig. 1B). Blood tests excluded acquired metabolic (including parathyroid hormone, calcium, phosphate and lactate), autoimmune, RPR, HIV antibody, and toxic (lead, mercury, cadmium, manganese and arsenic) causes of brain calcification.

Because of the characteristic brain features and lack of evidence of abnormalities in calcium or phosphate metabolism, PFBC was suspected. A genetic study with whole-exome sequencing was performed after informed consent was obtained from the patient. After the variants in the known PFBC-related genes were reviewed, a heterozygous missense variant, c.1891 C > T (p.Pro631Ser), in *SLC20A2*, which was not registered in gnomAD, dbSNP, ClinVar or the Taiwan Biobank, was detected and confirmed by Sanger sequencing (Fig. 1C). This missense variant affects a highly evolutionarily conserved amino acid residue (Fig. 1D). High probabilities of disruptive or deleterious effects on protein structure or function by residue substitution were predicted by CADD (score 25.9), SIFT (score 0, pathogenic), PolyPhen-2 (score 0.994, probably damaging) and AlphaMissense (score 0.9957).

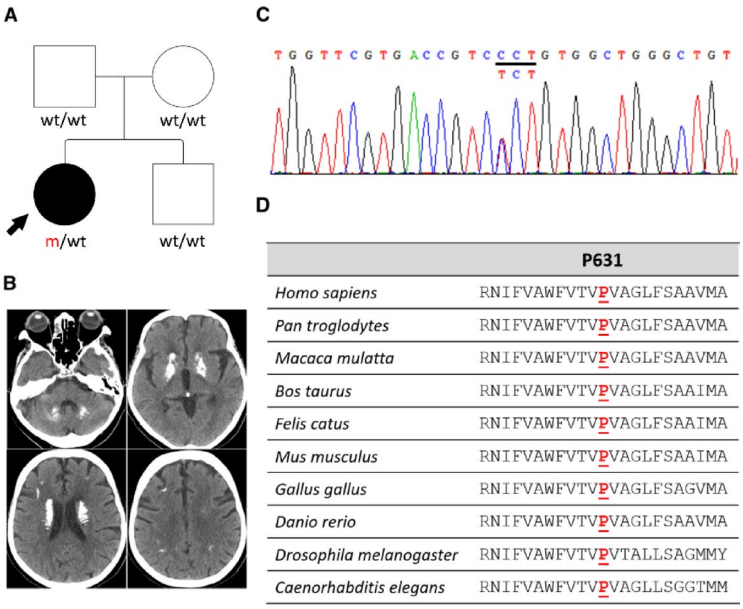

	P631
Homo sapiens	RNIFVAWFVTVPVAGLFSAAVMA
Pan troglodytes	RNIFVAWFVTVPVAGLFSAAVMA
Macaca mulatta	RNIFVAWFVTVPVAGLFSAAVMA
Bos taurus	RNIFVAWFVTVPVAGLFSAAIMA
Felis catus	RNIFVAWFVTVPVAGLFSAAIMA
Mus musculus	RNIFVAWFVTVPVAGLFSAAIMA
Gallus gallus	RNIFVAWFVTVPVAGLFSAGVMA
Danio rerio	RNIFVAWFVTVPVAGLFSAAVMA
Drosophila melanogaster	RNIFVAWFVTVPVTALLSAGMMY
Caenorhabditis elegans	RNIFVAWFVTVPVAGLLSGGTMM

Fig. 1. Clinical information and the detected *SLC20A2* mutation in the patient. (**A**) Pedigree with the proband indicated by an arrow. Squares represent male subjects, and circles represent female subjects. The affected individual is shown with solid symbols, and unaffected individuals or carriers are denoted with open symbols. (**B**) Brain CT image showing symmetric calcification in the bilateral dentate, basal ganglia and periventricular and subcortical white matter. (**C**) Electropherogram of the identified *SLC20A2* variant. wt, wild type; m, c.1891 C > T (p.Pro631Ser). (**D**) Conservation of the affected residue across different species.

The proband's parents and her brother exhibited normal neurological function and brain images and did not carry this *SLC20A2* variant (Fig. 1A). Paternity was confirmed via a panel of 15 microsatellite polymorphisms. Thus, the variant was interpreted as "likely pathogenic" (PS2, PM2, PP3, PP4) based on ACMG-AMP guidelines.

Secondary structures and molecular dynamics simulations

On the basis of the structure of TmPiT, which is homologous to the *h*PiT2 protein, we mapped the novel variant P631S and other variants in the TM8 helix, including V624E, W626 A, W626R, and S637R, to the *h*PiT2 TM domain (Fig. 2A).

To explore the effects of the *h*PiT2 variants on the TM8 helix, we modeled the structures of the *h*PiT2 variants V624E, W626A, W626R, P631S, and S637R. We then performed MD simulations on these mutants for 200 ns with three independent equilibrium simulations. We measured the root mean square deviation (RMSD) values to assess how these variants impact protein stability. Our results revealed that the average RMSD of the overall structure was 1.4 ± 0.1 Å for the WT protein and 1.4 ± 0.1 Å, 1.6 ± 0.2 Å, 1.8 ± 0.2 Å, 1.5 ± 0.2 Å, and 1.6 ± 0.1 Å for the V624E, W626A, W626R, P631S, and S637R mutant proteins, respectively (Fig. 2B). Since these variant residues are all embedded in the membrane, their overall structures remain similar. Nevertheless, the higher RMSD values for the *h*PiT2 variants suggested lower stabilities than those of the WT protein.

We next measured the kink angle of the TM8 helix by defining the upper (residues 626–631) and lower (residues 632–637) halves of TM8 as two representative vectors to evaluate the conformational change in TM8 (Fig. 3A). In *Tm*PiT, TM8 serves as a gate with a closed conformation to transport P_i within the membrane and an open conformation to allow the intracellular release of P_i[9]. We first measured the kink angles for TM8 of *Tm*PiT as 20.7° and 27.6° for the closed and open forms, respectively (Fig. 3B). After the MD simulations, we calculated the kink angles for the TM8 s of the WT and mutants of *h*PiT2. The most likely kink angle was 27.0° for the WT protein and 25.0°, 20.0°, 20.1°, 19.0°, and 22.0° for the five V624E, W626A, W626R, P631S, and S637R mutant proteins, respectively (Fig. 3B).

We subsequently compared the residual environments of these variants of *h*PiT2 within a 5 Å distance, with P_i shown as sticks and spheres in the binding site (Fig. 4). For wild-type *h*PiT2 (Fig. 4A), there is an important π-π interaction between W626 and H596 during P_i binding, which is conserved and found in *Tm*PiT[9]. In the V624E variant, the π-π interaction is absent because of the conformational change in the HP2 and TM8 helices. Moreover, the side chain of E624 may form a hydrogen bond with N621, potentially interfering with helix stability. As expected, the π-π interaction between W626 and H596 was lost in W626A and W626R mutants (Fig. 4C, D), and the hydrophobic environment around W626 was disrupted under these conditions (Fig. 4D). Furthermore, as W626R forms a hydrogen bond with S113, which corresponds to one of the Pi/Na binding residues in *Tm*PiT[9], the W626R mutation may perturb this critical role of S113. For P631S, the variant present in our case, the replacement of a pyrrolidine ring by a hydroxymethyl side chain, which resists approaching the lipid environment, may result in TM8 toward a closed conformation, and stacking the additional π-π interactions between H116 and H596 (Fig. 4E). In the S637R mutant protein, the π-π interaction between H596 and W626 is retained, and the mutated arginine forms a hydrogen bond with E91 (Fig. 4F). Although E91 is not a highly conserved residue in the PiT family, this interaction may flip F125 outward from the HP1 helix (Fig. 4F).

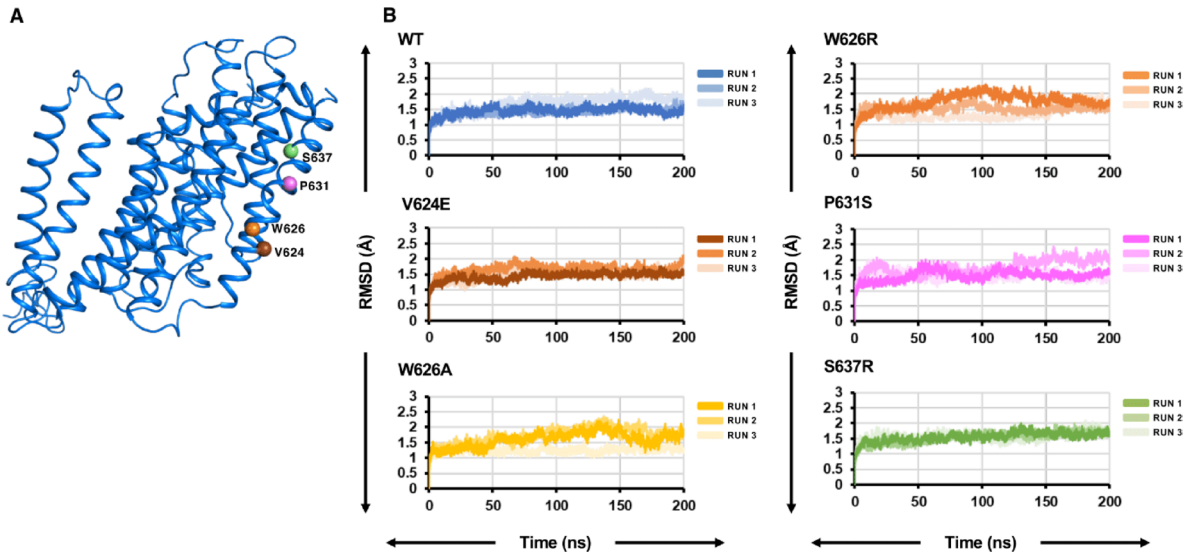

Fig. 2. Initial structure and molecular dynamics of *h*PiT2. (**A**) The transmembrane domain of *h*PiT2 constructed on the basis of *Tm*PiT, with residues V624, W626, P631, and S637 mapped to the structure. (**B**) Root mean square deviation (RMSD) values of the wild-type and V624E, W626A, W626R, P631S, and S637R mutant *h*PiT2 structures.

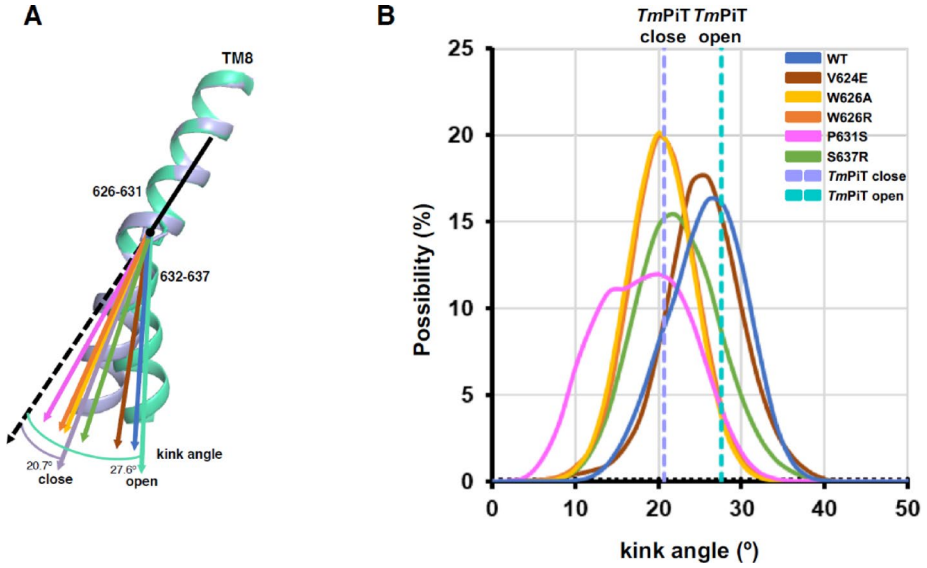

Fig. 3. Measurement of the TM8 helix kink angles. (**A**) The kink angle of the TM8 helix is measured by defining two representative vectors. The upper half is defined with residues 626 to 631, and the lower half is defined with residues 632 to 637. (**B**) The measured *Tm*PiT kink angles in the open (27.6°) and closed (20.7°) states and the wild-type and mutant *h*PiT2 kink angles were observed using molecular dynamic simulations. The most likely kink angle of the P631S mutant is 19.0°, which is the lowest among all the *h*PiT2 mutants. This mutant also has the widest range of possible kink angles.

In summary, these mutants of *h*PiT2, including P631S, may destabilize the protein, reduce the kink angle of TM8, disturb the hydrophobicity of TM8 and its associated TM helices, and potentially cause dysfunctional P_i binding and transport for *h*PiT2.

Discussion

The clinical features of PFBC are heterogeneous. The pathogenesis of neurological and psychiatric symptoms in PFBC-*SLC20A2* patients could be multifactorial. Several plausible mechanisms, including cerebral hypoperfusion due to microvasculopathy[18], impairment of dopaminergic pathways[25], cellular energy deficiency due to mitochondrial dysfunction[26], and reactivation of astrocytes and microglia[27], have been implicated in brain damage. *h*PiT2 is expressed ubiquitously in various tissues, with the highest levels noted in the basal ganglia, thalamus and cerebellum[28]. In combination with the other human PiT family member *h*PiT1, *h*PiT2 maintains cerebral P_i homeostasis. In the choroid plexus, *h*PiT2 is localized mainly in the apical microvillar membranes facing the cerebrospinal fluid, contributing to the transport of P_i from the cerebrospinal fluid to the blood[29]. The perturbation of *h*PiT2 functions leads to impaired intracellular P_i import and subsequent anomalous calcium phosphate deposition due to extracellular P_i accumulation[12].

On the basis of the model we established previously, *Tm*PiT is a dimer in which each subunit includes a transport domain and a scaffold domain composed of 12 TM helices. The transport domain is formed by two inverted repeats, N-PD001131 and C-PD001131[9]. The TM8 helix is located in the C-PD001131 repeat. By adopting conformation changes, the helix governs the opening of the transporter inner gate and plays an important role in controlling intracellular P_i entry, highlighting the role of TM8 in *h*PiT2 function. A highly conserved residue W378 of *Tm*PiT (corresponding to W626 in *h*PiT) located in the middle of TM8 is hypothesized to be involved in TM8 bending for inner gate opening[9]. In support of this, *Tm*PiT with the W378A mutation loses its P_i-binding ability, and the *SLC20A2* variant W626R is associated with PFBC[9,17].

By providing important information on how molecular characteristics of the protein are affected upon mutation, computational simulations of molecular dynamics can serve as supplementary investigations for cellular or animal models to predict the pathogenicity of mutant protein[30]. To assess the pathogenicity of the variant P631S, the stability of the entire TM domain was first tested via MD simulation. We showed that variant P631S had a greater RMSD, which implied a lower molecular stability than that of WT *h*PiT2. Additionally, the simulation of the TM8 kink angle revealed that the P631S variant had a wider predicted kink angle range than WT *h*PiT2 did (Fig. 3B). This finding suggests that serine may introduce a more malleable structure compared to proline. However, the π-π stacking interactions among H116, H596, and W626 restricted the kink angle and maintained in the closed conformation of TM8. Next, as the P631 residue is located in the TM8 helix of *h*PiT2, the influence of the variant on the kink angle of TM8 was evaluated. Among the amino acids, proline and glycine are known to disrupt helix formation in the secondary structure[31]. A lack of an amide hydrogen prevents proline from forming a helix, which facilitates the introduction of a kink in an amino acid chain[32]. This property is significant in many membrane proteins, where proline acts as a ligand-binding site for cations[33]. Moreover, proline commonly serves as a molecular switch involved in conformational changes, as observed in transporters such as NaDT and LeuT[34]. The P631 residue is positioned centrally within the membrane and located in the

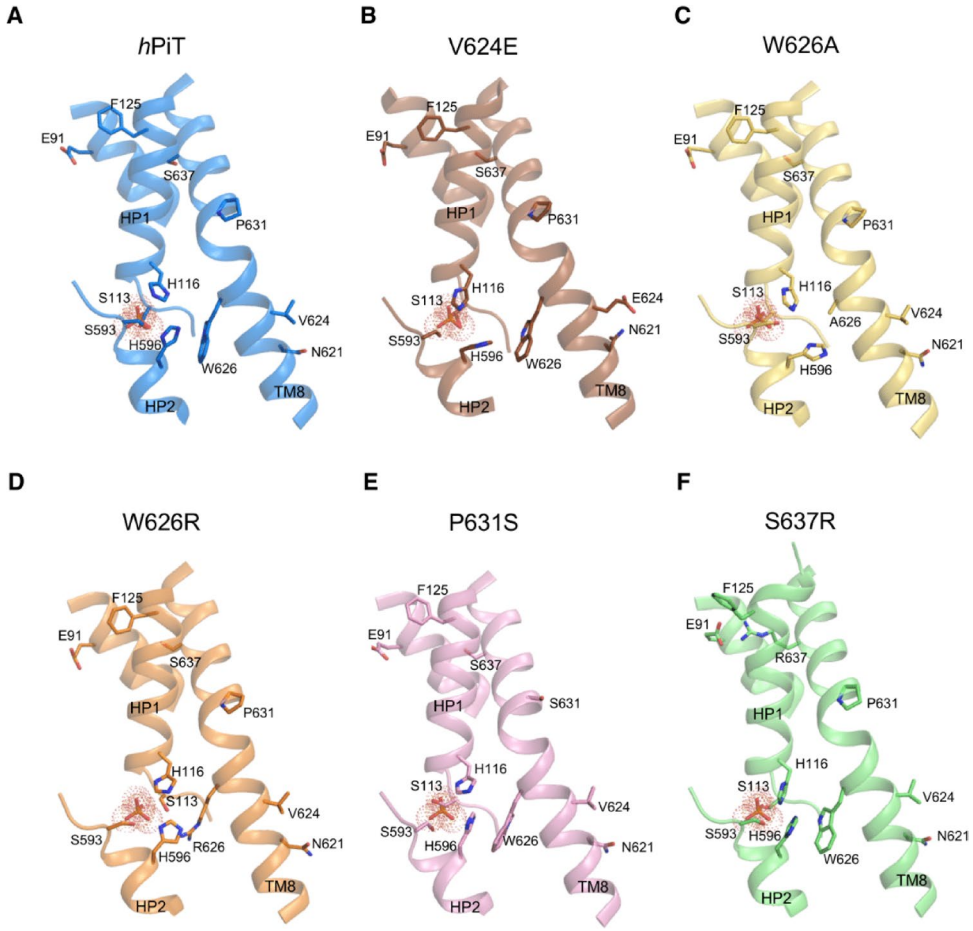

Fig. 4. Residual environments of wild-type and mutant *h*PiT2. (**A**-**F**) An important π-π interaction between W626 and H596 during P_i binding in wild-type *h*PiT2 is lost in the V624E, W626A, and W626R mutants. A new hydrogen bond is formed between the mutated residue in the V624E mutant and N621, and a similar situation is observed between the mutated residue S637R and E91. A pyrrolidine ring side chain pointed toward the lipid environment in the P631S mutant is lost.

middle of the TM8 helix, suggesting that it might be a bending site of this helix. Our study revealed that the simulated TM8 kink angle of WT *h*PiT2 is 27.0°, whereas that of the P631S variant is only 19.0°, suggesting that the flexion of the TM8 helix may be reduced by this amino acid change. Finally, scrutiny of the sequence homology and helical wheel projection of TM8 (Additional File 2) revealed only two polar residues, T629 and S637, indicating that TM8 is a very hydrophobic helix. TM8 is located between the substrate binding site and the membrane lipid. Residue P631 and a series of spatially adjacent residues form a highly hydrophobic region composed of 624(I/M/V)–628(L/V)–631P-635(A/V/L)–639 A on the lipid side of TM8. Replacement of the hydrophobic residue by a charged or polar residue, as in the cases of V624E and P631S, may alter the integrity of the interface between the hydrophobic region and the lipid membrane. We conclude that the P631S mutation may alter the flexibility of the TM domain and the conformation of the TM8 helix, potentially impairing the P_i transport functions of *h*PiT2. The pathogenicity of the novel variant P631S is further supported by similar changes in TM domain flexibility and the TM8 kink angle, which are also present in the missense variants in TM8 associated with PFBC clinically (V624E, W626R, S637R) or impaired P_i transport of *h*PiT2 in vitro (W626A) (Figs. 2B, 3B and 4).

It should be noted that our study is limited to computational modeling and molecular dynamics simulation for effects of amino acid substitution on protein 3D structure and stability. Additional in vitro or in vivo studies are needed to confirm the findings and their associations with *h*PiT2 functions.

Conclusions

We present a novel and rarely found *de novo SLC20A2* variant, c.1891 C > T (p.Pro631Ser), in a PFBC patient. Based on computational modeling and simulations, its pathogenicity is supported by comparisons with wild-type *h*PiT2 as well as known disease-causing or functionally deleterious variants in the same functional region. Our findings also highlight the role of the TM8 helix in *h*PiT2 functions.

Data availability

The datasets generated and/or analyzed during the current study are available in the figshare repository at https://figshare.com/articles/figure/A_SLC20A2_novel_and_de_novo_variant_associated_with_PFBC/27215568.

Received: 18 November 2024; Accepted: 23 May 2025
Published online: 28 May 2025

References

1. Carecchio, M., Mainardi, M. & Bonato, G. The clinical and genetic spectrum of primary Familial brain calcification. *J. Neurol.* **270** (6), 3270–3277 (2023).
2. Ramos, E. M., Oliveira, J., Sobrido, M. J. & Coppola, G. in *Primary Familial Brain Calcification in GeneReviews®*. (eds Adam, M. P.) (University of Washington, 2004).
3. Yao, X. P. et al. Biallelic mutations in MYORG cause autosomal recessive primary Familial brain calcification. *Neuron* **98** (6), 1116–1123e5 (2018).
4. Schottlaender, L. V. et al. Bi-allelic JAM2 variants lead to Early-Onset recessive primary Familial brain calcification. *Am. J. Hum. Genet.* **106** (3), 412–421 (2020).
5. Zhao, M. et al. Loss of function of CMPK2 causes mitochondria deficiency and brain calcification. *Cell. Discov.* **8** (1), 128 (2022).
6. Chelban, V. et al. Biallelic NAA60 variants with impaired n-terminal acetylation capacity cause autosomal recessive primary Familial brain calcifications. *Nat. Commun.* **15** (1), 2269 (2024).
7. Yamada, M. et al. Evaluation of SLC20A2 mutations that cause idiopathic basal ganglia calcification in Japan. *Neurology* **82** (8), 705–712 (2014).
8. Balck, A. et al. Genotype-Phenotype relations in primary Familial brain calcification: systematic MDSGene review. *Mov. Disord.* **36** (11), 2468–2480 (2021).
9. Tsai, J. Y. et al. Structure of the sodium-dependent phosphate transporter reveals insights into human solute carrier SLC20. *Sci. Adv.* **6** (32), eabb4024 (2020).
10. Salaün, C., Rodrigues, P. & Heard, J. M. Transmembrane topology of PiT-2, a phosphate transporter-retrovirus receptor. *J. Virol.* **75** (12), 5584–5592 (2001).
11. Bøttger, P. & Pedersen, L. Mapping of the minimal inorganic phosphate transporting unit of human PiT2 suggests a structure universal to PiT-related proteins from all kingdoms of life. *BMC Biochem.* **12**, 21 (2011).
12. Wang, C. et al. Mutations in SLC20A2 link Familial idiopathic basal ganglia calcification with phosphate homeostasis. *Nat. Genet.* **44** (3), 254–256 (2012).
13. Ferreira, J. B. et al. First report of a de Novo mutation at SLC20A2 in a patient with brain calcification. *J. Mol. Neurosci.* **54** (4), 748–751 (2014).
14. Sellami, L., Verret, L., Poulin, S. & Laforce, R. Fahr's disease due to a novel SLC20A2 gene mutation in a Canadian patient: early neurocognitive, structural and metabolic changes (P2.175). *Neurology* (2018). 90 (15_supplement).
15. Abramson, J. et al. Accurate structure prediction of biomolecular interactions with alphafold 3. *Nature* **630** (8016), 493–500 (2024).
16. Ramos, E. M. et al. Primary brain calcification: an international study reporting novel variants and associated phenotypes. *Eur. J. Hum. Genet.* **26** (10), 1462–1477 (2018).
17. Chen, S. et al. Underestimated disease prevalence and severe phenotypes in patients with biallelic variants: A cohort study of primary Familial brain calcification from China. *Parkinsonism Relat. Disord.* **64**, 211–219 (2019).
18. Kimura, T. et al. Familial idiopathic basal ganglia calcification: histopathologic features of an autopsied patient with an SLC20A2 mutation. *Neuropathology* **36** (4), 365–371 (2016).
19. Anashkin, V. A. & Baykov, A. A. A lumenal loop associated with catalytic asymmetry in plant vacuolar H+-Translocating pyrophosphatase. *Int. J. Mol. Sci.* **22** (23), 12902 (2021).
20. Jo, S., Kim, T. & Im, W. Automated builder and database of protein/membrane complexes for molecular dynamics simulations. *PLoS One* **2**(9), e880 (2007).
21. Jo, S., Kim, T., Iyer, V. G. & Im, W. CHARMM-GUI: a web-based graphical user interface for CHARMM. *J. Comput. Chem.* **29** (11), 1859–1865 (2008).
22. Shah, N. R. et al. Insights into the mechanism of membrane pyrophosphatases by combining experiment and computer simulation. *Struct. Dyn.* **4** (3), 032105 (2017).
23. Maier, J. A. et al. ff14SB: improving the accuracy of protein side chain and backbone parameters from ff99SB. *J. Chem. Theory Comput.* **11** (8), 3696–3713 (2015).
24. Case, D. A. et al. AmberTools. *J. Chem. Inf. Model.* **63** (20), 6183–6191 (2023).
25. Koyama, S. et al. Clinical and radiological diversity in genetically confirmed primary Familial brain calcification. *Sci. Rep.* **7** (1), 12046 (2017).
26. Sun, H. et al. Golgi damage caused by dysfunction of PiT-2 in primary Familial brain calcification. *Biochem. Biophys. Res. Commun.* **642**, 167–174 (2023).
27. Nahar, K. et al. Astrocyte-microglial association and matrix composition are common events in the natural history of primary Familial brain calcification. *Brain Pathol.* **30** (3), 446–464 (2020).
28. da Silva, R. J., Pereira, I. C. & Oliveira, J. R. Analysis of gene expression pattern and neuroanatomical correlates for SLC20A2 (PiT-2) shows a molecular network with potential impact in idiopathic basal ganglia calcification (Fahr's disease). *J. Mol. Neurosci.* **50** (2), 280–283 (2013).
29. Guerreiro, P. M., Bataille, A. M., Parker, S. L. & Renfro, J. L. Active removal of inorganic phosphate from cerebrospinal fluid by the choroid plexus. *Am. J. Physiol. Ren. Physiol.* **306** (11), F1275–F1284 (2014).
30. Mir, Y. R. et al. Identification and structural characterization of a pathogenic ARSA missense variant in two consanguineous families from Jammu and Kashmir (India) with late infantile metachromatic leukodystrophy. *Mol. Biol. Rep.* **51** (1), 30 (2023).
31. Cordes, F. S., Bright, J. N. & Sansom, M. S. Proline-induced distortions of transmembrane helices. *J. Mol. Biol.* **323** (5), 951–960 (2002).
32. Wilman, H. R., Shi, J. & Deane, C. M. Helix Kinks are equally prevalent in soluble and membrane proteins. *Proteins* **82** (9), 1960–1970 (2014).
33. Sansom, M. S. Proline residues in transmembrane helices of channel and transport proteins: a molecular modelling study. *Protein Eng.* **5** (1), 53–60 (1992).
34. Kahn, E. S. & Pajor, A. M. Determinants of substrate and cation affinities in the Na+/dicarboxylate cotransporter. *Biochemistry* **38** (19), 6151–6156 (1999).

Acknowledgements

We are grateful to the patient and family members who participated in this study. This work was supported by the National Science and Technology Council, Taiwan (NSTC 111-2326-B-007-001- and 113-2311-B-007-007-MY3 to Y.-J. S.)

Author contributions

S.C.L., Y.J.S., and Y.Y.C.: study conceptualization and design. Y.S.H., J.Y.T., M.Y.L., and Y.Y.C.: data collection. S.C.L. and M.Y.L.: genetic testing and data analysis. Y.S.H., J.Y.T. and Y.J.S.: molecular structure modeling, molecular dynamics simulation and data analysis. S.C.L., Y.S.H., J.Y.T. and Y.Y.C.: writing of the first draft. M.Y.L. and Y.J.S.: manuscript review and critique.

Funding

This work was supported by the National Science and Technology Council, Taiwan (NSTC 111-2326-B-007-001- and 113-2311-B-007-007-MY3 to Y.-J. S.)

Declarations

Competing interests

The authors declare no competing interests.

Consent for publication

Written informed consent was obtained from the patient for the publication of this case report and any accompanying images.

Additional information

Supplementary Information The online version contains supplementary material available at https://doi.org/10.1038/s41598-025-03953-1.

Correspondence and requests for materials should be addressed to Y.-J.S. or Y.-Y.C.

Reprints and permissions information is available at www.nature.com/reprints.

Publisher's note Springer Nature remains neutral with regard to jurisdictional claims in published maps and institutional affiliations.